Interplay of induced charge electroosmosis and electrothermal flow in insulator-based dielectrophoresis

Amirreza Malekanfard [1,*] Zhijian Liu [1,2,*] Hui Zhao [3]
Yongxin Song [2,†] and Xiangchun Xuan [1,‡]

[1]*Department of Mechanical Engineering, Clemson University, Clemson, South Carolina 29634-0921, USA*
[2]*College of Marine Engineering, Dalian Maritime University, Dalian 116026, China*
[3]*Department of Mechanical Engineering, University of Nevada, Las Vegas, Nevada 89154, USA*

Insulator-based dielectrophoresis (iDEP) is an emerging technique for particle manipulation in microfluidic devices. Two nonlinear electrokinetic flows have been demonstrated to take place simultaneously in iDEP: one is induced charge electroosmosis (ICEO) due to the electric polarization of the insulator, and the other is electrothermal flow (ETF) due to the amplified Joule heating of the fluid around the insulator. These flows vary differently with the applied electric field, and become strong in a fluid with a low and a high electric conductivity, respectively. They both exhibit the pattern of fluid vortices near the insulator but with opposite circulating directions. We present in this work an experimental study of the interplay of ICEO and ETF in a constricted microchannel under dc-biased ac voltages. We also develop a depth-averaged numerical model to simulate the coupled electrokinetic fluid flow with the charge and energy transport. The experimentally measured nonlinear fluid velocity agrees closely with the numerical prediction for both a wide range of buffer concentrations and a range of ac voltages. It also matches asymptotically the predicted velocity of ICEO in a low-concentration buffer under a small ac voltage and that of ETF in a high-concentration buffer, both of which are consistent with a scaling analysis. Interestingly, the nonlinear fluid velocity becomes marginal in moderate-concentration buffers under moderate ac voltages because of the opposing effects of ICEO and ETF.

I. INTRODUCTION

Insulator-based dielectrophoresis (iDEP) has been increasingly used to focus, trap, and sort various types of particles (e.g., colloids, cells, viruses, molecules, etc.) for microfluidic applications [1–5]. This technique utilizes insulating structure(s), which is often made of the same material [e.g., polydimethylsiloxane (PDMS), polymethyl methacrylate (PMMA), and glass] as the microchannel itself, to create electric field gradients for a nonlinear dielectrophoretic manipulation in addition to the linear electrokinetic motion of particles [6–10]. However, the presence of insulator(s) within the fluid has been demonstrated to generate two nonlinear electrokinetic flows that may suppress or enhance the performance of iDEP [11]: one is induced charge electroosmosis (ICEO) that arises from the electric polarization of the insulator because of its small but finite permittivity [see a schematic illustration in Fig. 1(a)] [12], and the other is electrothermal flow (ETF) that results from the action of the applied electric field on the fluid property gradients caused by the locally amplified Joule heating effect around the insulator [see a schematic illustration in Fig. 1(b)] [13].

---

[*]These authors contributed equally to this work.
[†]Corresponding author: yongxin@dlmu.edu.cn
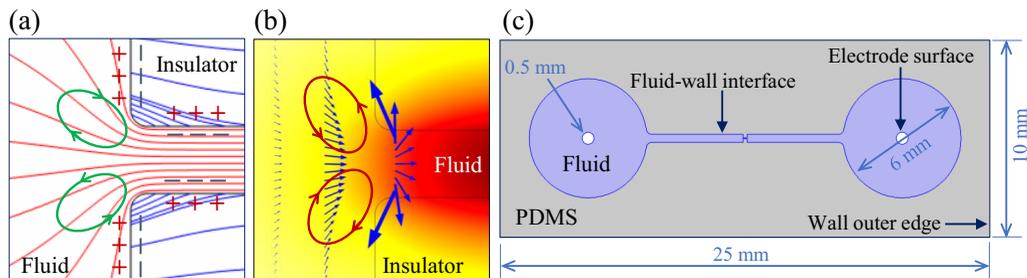[‡]Corresponding author: xcxuan@clemson.edu

FIG. 1. (a) Schematic illustrating the formation of ICEO (highlighted by the looped arrows) around the corners of insulators in an iDEP microdevice because of the action of electric field upon the diffuse charge induced by the leaked electric field (see the background lines) into the insulator; (b) schematic illustrating the formation of ETF (highlighted by the looped arrows) around the corners because the action of electric field upon the Joule heating-induced fluid property gradients (see the background color, the darker the higher temperature) creates an electrothermal force (see the vector plot); (c) schematic showing the geometry and computational domain of the constricted microchannel used in this work.

The velocity of ICEO varies with the second order of electric field [14–17] while that of ETF is a fourth-order function of electric field [18–20]. Both flows exhibit the pattern of fluid vortices near the insulator but with opposite circulating directions [11]. They have each been fundamentally investigated (specifically, ICEO [21–25] and ETF [26–30]) as well as being utilized for microfluidic applications (e.g., pumping and mixing by ICEO [31–35] as well as trapping and enrichment by ETF [36–41]) if available. A summary of the work on nonlinear electrokinetic flows in iDEP microdevices can be referred to a recent review article [11].

However, the majority of the existing studies has been focused upon ICEO and ETF separately despite that the two fluid flows take place simultaneously in iDEP devices [11]. Thus far, there are only a couple of papers concerning the interplay of ICEO and ETF. Zehavi *et al.* [42] performed an experimental and numerical investigation of ICEO in buffer solutions with varying concentrations at the sharp corner of an L-shaped PDMS microchannel in the presence of Joule heating effects. The authors employed ac electric field to remove the influence of the linear electroosmotic background flow and hence isolate the nonlinear ICEO ejection flow. They reported an increasing divergence from the standard ICEO flow with the increase of the buffer concentration (and in turn the electric conductivity), which was demonstrated to result from the enhanced electrothermal effect. In another work, Wang *et al.* [43] reported an experimental and theoretical study on the interplay of ICEO and ETF in fluids with various ionic strengths under ac electric fields near both a two-dimensional (2D) (widthwise) PDMS and a 3D (both width- and depthwise) PMMA microchannel constriction. They observed qualitatively distinct recirculating flow patterns in the 2D and 3D geometries. Moreover, the authors obtained approximately analytical expressions for the ICEO and ETF velocity scales as a function of the key design parameters in iDEP microdevices. They further demonstrated that the effects of ICEO and ETF can dominate over that of DEP under a wide range of circumstances encountered in iDEP devices.

We present in this work an experimental study of the nonlinear fluid flow in a typical iDEP microdevice [1–5], a 2D constricted PDMS microchannel. Considering that dc or dc-biased ac voltages are often used in iDEP devices for both the dc electrokinetic pumping and dc or ac dielectrophoretic manipulation of particles [6–10], we employ dc-biased ac voltages in our experiment. To examine the interplay of ICEO and ETF, we vary the buffer concentration by nearly three orders of magnitude. The applied ac voltage is also varied in every buffer solution to achieve the transition from ICEO to ETF if available. Moreover, we develop a depth-averaged numerical model to account for both the electric polarization and Joule heating effects on the coupled electrokinetic fluid flow with the charge and energy transport. The predicted nonlinear fluid velocity is compared with the

experimental measurement as well as the predicted velocities of ICEO and ETF, respectively. The comparison is backed up by a scaling analysis.

II. METHOD

A. Experiment

Figure 1(c) shows a schematic representation of the iDEP microdevice that was fabricated with PDMS using the standard soft lithography method [44]. The microchannel is 1 cm long and 400 μm wide with a 200-μm-long and 40-μm-wide constriction in the middle. It has a uniform depth of 40 μm. To visualize the fluid motion, 1-μm-diameter spherical polystyrene particles (Polysciences, Inc.) were seeded into phosphate buffer solutions with the concentration ranging from 0.01 to 5 mM, which were prepared by diluting the stored 100-mM phosphate buffer (75.4 mM $Na_2HPO_4 \bullet 7H_2O$ and 24.6 mM $NaH_2PO_4 \bullet H_2O$) with DI water. dc-biased ac electric voltages were supplied by a function generator (33220A, Agilent Technologies) in conjunction with a high-voltage amplifier (609E-6, Trek). The dc voltage was fixed at 20 V while the ac voltage of 1 kHz was varied in the test of each buffer solution. Images were captured with an inverted microscope (Nikon Eclipse TE2000U, Nikon Instruments) through a charge-coupled device camera (Nikon DS- Qi1Mc), and postprocessed in the Nikon imaging software (NIS-Elements AR 3.22). The particle velocity was obtained from the image series by tracking the motion of individual particles with time, and was averaged over at least three particles for each tested case.

The electric conductivity of the prepared buffer solutions was measured using a conductivity meter (Fisher Scientific). The average equilibrium zeta potential of the PDMS or glass walls in contact with each buffer solution was measured using the standard electric current monitoring method in a straight uniform microchannel [45]. Also measured in the same microchannel is the electrokinetic particle mobility via single particle tracking. Combining these two sets of data gives the particle zeta potentials in buffer solutions of varying concentrations. The obtained dependencies of the room-temperature fluid conductivity σ_0 (μS/cm), wall zeta potential ζ_w (mV), and particle zeta potential ζ_p (mV) on the buffer concentration c (mM) are given by

$$\sigma_0 = 200c, \tag{1}$$

$$\zeta_w = -40 + 30\log_{10}(c), \tag{2}$$

$$\zeta_p = -60 + 9\log_{10}(c). \tag{3}$$

It is important to note that the electrokinetic particle mobility switches from along the dc electric field (defined as the positive direction for both the fluid and particle velocities hereon) to against it (defined as the negative direction) at the buffer concentration of around 0.1 mM. The trend of our measured zeta potentials with respect to the buffer concentration is found consistent with the reported data in the literature [46,47]. Other fluid properties such as permittivity, viscosity, and thermal conductivity are assumed independent of the buffer concentration and equal to the values of water.

B. Model

The simulation of ICEO and ETF in iDEP microdevices involves the consideration of fluid, electric charge, and energy transport, where the latter two take place in both the fluid and solid (i.e., the PDMS walls) domains. The depth-averaged governing equations for these transport phenomena in the horizontal plane of the microchip [see Fig. 1(c) for the computational domain] are summarized below, where the detailed process for the associated asymptotic analysis [48,49] can be referred to

our recent papers [25,30,50]. The electric field is solved in both the fluid and the PDMS walls [20,48,51],

$$\nabla_H \cdot (\sigma \mathbf{E}_f) = 0, \tag{4}$$

$$\nabla_H \cdot (\varepsilon_w \mathbf{E}_w) = 0, \tag{5}$$

where ∇_H denotes the vector differential operator in the horizontal plane of the microchip, σ is the electrical conductivity of the fluid, $\mathbf{E}_f$ is the electric field in the fluid, ε_w is the permittivity of the wall, and $\mathbf{E}_w$ is the electric field in the wall. At the fluid-wall interface, the Robin type boundary condition is used to consider the electric potential jump from the fluid to the wall [52–54],

$$\phi_w - \phi_f = \zeta_w + \zeta_i, \tag{6}$$

$$\zeta_i = \lambda \frac{\varepsilon_w}{\varepsilon_f} \mathbf{E}_w \cdot \mathbf{n}, \tag{7}$$

$$\lambda = \sqrt{\frac{\varepsilon_f RT}{2z^2 F^2 c}}, \tag{8}$$

where ϕ_w and ϕ_f are, respectively, the electric potentials in the wall and fluid with the definitions of $\mathbf{E}_f = -\nabla\phi_f$ and $\mathbf{E}_w = -\nabla\phi_w$, ζ_w is the equilibrium zeta potential of the wall, ζ_i is the wall polarization-induced zeta potential, λ is the Debye length, ε_f is the permittivity of the fluid, $\mathbf{n}$ is the unit normal vector of the wall, R is the universal gas constant, T is the fluid temperature, z is the ionic valence (assumed unity here), F is the Faraday constant, and c is the fluid ionic concentration. Other boundary conditions for the electric field equations include the electric insulation at the wall outer edge and the voltage on each electrode surface [see Fig. 1(c)].

The flow field is governed by the Navier-Stokes equations [25,30,50],

$$\rho_f \left[\frac{\partial \mathbf{u}}{\partial t} + (\mathbf{u} \cdot \nabla_H)\mathbf{u} \right] = -\nabla_H p + \nabla_H \cdot (\eta\nabla_H \mathbf{u}) + \mathbf{f}_e - \frac{3\eta}{d^2}(\mathbf{u} - \mathbf{u}_{EO}), \tag{9}$$

$$\langle \mathbf{f}_e \rangle = [\nabla_H \cdot (\varepsilon_f \mathbf{E}_f)]\mathbf{E}_f - \tfrac{1}{2}\mathbf{E}_f^2 \nabla_H \varepsilon_f, \tag{10}$$

$$\nabla_H \cdot \mathbf{u} = 0, \tag{11}$$

where ρ_f is fluid density, $\mathbf{u}$ is the fluid velocity, t is the time, p is the hydrodynamic pressure, η is the fluid viscosity, $\langle \mathbf{f}_e \rangle$ is the electrothermal force consisting of the Coulomb and dielectric components [20,55], d is the half depth of the microchannel, and $\mathbf{u}_{EO} = -\varepsilon_f \zeta_w \mathbf{E}_{f\_dc}/\eta$ is the average electroosmotic slip velocity on the top and bottom walls of the microchannel with $\mathbf{E}_{f\_dc}$ being the component of dc electric field. Note that the last term on the right hand side of the flow equation accounts for the influence of the top and bottom walls on the depth-averaged flow field. Under the thin EDL limit (as compared to the channel dimensions) [56,57], we apply a slip condition, $\mathbf{u} \cdot \mathbf{t} = -\varepsilon_f(\zeta_i + \zeta_w)\mathbf{E}_{f\_dc} \cdot \mathbf{t}/\eta$, at the fluid-wall interface and a nonslip condition on each electrode surface [see Fig. 1(c)].

The temperature field is governed by the energy equation in the fluid and walls, respectively [30,41,42,58],

$$\rho_f C_{Pf} \left(\frac{\partial T}{\partial t} + \mathbf{u} \cdot \nabla_H T \right) = \nabla_H \cdot (k_f \nabla_H T) + \sigma \mathbf{E}_f^2 - \frac{T - T_0}{2d}\left(\frac{1}{R_{\text{top}}} + \frac{1}{R_{\text{bot}}} \right), \tag{12}$$

$$\rho_{\text{PDMS}} C_{P\text{PDMS}} \frac{\partial T}{\partial t} = \nabla_H \cdot (k_{\text{PDMS}} \nabla_H T) - \frac{T - T_0}{2d}\left(\frac{1}{R_{\text{top}}} + \frac{1}{R_{\text{bot}}} \right), \tag{13}$$

where ρ, C_p, and k are the mass density, heat capacity, and thermal conductivity of the fluid (with the subscript f) or walls (with the subscript PDMS), respectively, T_0 is the room temperature, and $R_{\text{top}} = t_{\text{PDMS}}/k_{\text{PDMS}} + 1/h$ and $R_{\text{bot}} = t_{\text{glass}}/k_{\text{glass}}$ are the equivalent thermal resistances of the top and bottom channel walls per unit area with t_{PDMS} (t_{glass}) being the thickness of the top PDMS (bottom glass) wall and h the natural convection coefficient [42]. Note that the Joule heating term $\sigma \mathbf{E}_f^2$ is only present in the energy equation for the fluid domain because of the assumed zero electric conductivity of the walls [58,59]. The last term on the right hand side accounts for the heat dissipation from the top and bottom channel walls [42]. An isothermal condition at T_0 is imposed upon the electrode surface and the outer edge of the walls is exposed to a natural convection with the coefficient h.

The above depth-averaged equations are coupled through temperature dependent fluid properties [59,60],

$$\varepsilon_f = \varepsilon_{f0}[1 + \alpha(T - T_0)], \tag{14}$$

$$\sigma = \sigma_0[1 + \beta(T - T_0)], \tag{15}$$

$$\eta = 2.671 \times 10^{-6} \exp\left(\frac{1713}{T}\right), \tag{16}$$

where ε_{f0} and σ_0 are the fluid permittivity and electric conductivity at the room temperature with α and β being their respective temperature coefficients. These equations were solved at steady state in the horizontal plane of the iDEP microchip [see Fig. 1(c)] using COMSOL® Multiphysics 5.5. Note that the temperature dependences of the boundary conditions [e.g., the Debye length in Eq. (8) and electroosmotic slip velocity] were also included in the model. Following the treatment in our earlier papers [28–30,38,41], we neglected the temperature dependence of all other properties in the model. The streak lines of tracing particles were simulated using the particle velocity,

$$\mathbf{u}_p = \mathbf{u} + \mathbf{u}_{\text{EP}} + \mathbf{u}_{\text{DEP}} \tag{17}$$

where $\mathbf{u}_{\text{EP}} = \varepsilon_f \zeta_p \mathbf{E}_{f\_dc}/\eta$ is the electrophoretic particle velocity and $\mathbf{u}_{\text{DEP}} = \frac{\varepsilon_f a^2}{3\eta} \frac{\sigma_p - \sigma}{\sigma_p + 2\sigma} \nabla \mathbf{E}_f^2$ is the dielectrophoretic particle velocity with ζ_p, a, and σ_p being the particle's zeta potential, radius, and electric conductivity, respectively. Table I summarizes the material properties used in the model unless otherwise stated elsewhere.

C. Scaling analysis

Referring to the induced zeta potential ζ_i in Eq. (7), and the Debye length λ in Eq. (8) we may estimate the speed of ICEO as

$$U_{\text{ICEO}} = \frac{\varepsilon_f \zeta_i}{\eta} E_f = \lambda \frac{\varepsilon_w}{\eta} E_f E_w \sim \varepsilon_w \sqrt{\varepsilon_f} \frac{E_f^2}{\sqrt{c}}, \tag{18}$$

which is a quadratic function of the applied electric field and gets stronger with the decrease of the fluid ionic concentration. In contrast, the electrothermal force $\mathbf{f}_e$ in Eq. (10) for small fluid temperature rises is simplified to [18]

$$\langle \mathbf{f}_e \rangle = \frac{1}{2}\left[\left(\frac{\nabla \varepsilon_f}{\varepsilon_f} - \frac{\nabla \sigma}{\sigma} \right) \cdot \mathbf{E}_f \right] \varepsilon_f \mathbf{E}_f - \frac{1}{4}\mathbf{E}_f^2 \nabla \varepsilon_f. \tag{19}$$

Further considering $\nabla \varepsilon_f = \varepsilon_{f0} \alpha \nabla T \approx \varepsilon_f \alpha \nabla T$ and $\nabla \sigma = \sigma_0 \beta \nabla T \approx \sigma \beta \nabla T$ for small fluid temperature rises, we can rewrite the last equation as

$$\langle \mathbf{f}_e \rangle \approx \frac{1}{2}(\alpha - \beta)(\nabla T \cdot \mathbf{E}_f)\varepsilon_f \mathbf{E}_f - \frac{1}{4}\varepsilon_f \mathbf{E}_f^2 \alpha \nabla T. \tag{20}$$

TABLE I. Summary of the parameters and material properties in the simulation.

Symbol	Value	Unit	Description
ρ_f	1000	Kg/m^3	fluid mass density
k_f	0.61	W/(m K)	fluid thermal conductivity
C_{pf}	4.18	kJ/(kg K)	fluid heat capacity
β	0.02	1/K	temperature coefficient of fluid electric conductivity
ε_{f0}	7.10×10^{-10}	F/m	fluid permittivity at room temperature
α	-0.0046	1/K	temperature coefficient of fluid permittivity
ρ_{PDMS}	970	Kg/m^3	PDMS mass density
k_{PDMS}	0.61	W/(m K)	PDMs thermal conductivity
$C_{P\mathrm{PDMS}}$	1.46	kJ/(kg K)	PDMs heat capacity
t_{PDMS}	3	mm	PDMS slab thickness
k_{PDMS}	0.15	W/(m K)	PDMS thermal conductivity
ε_w	3.54×10^{-11}	F/m	PDMS permittivity
t_{glass}	1	Mm	glass slide thickness
k_{glass}	1.38	W/(m K)	glass thermal conductivity
d	20	μm	half-depth of the microchannel
T_0	293.15	K	room temperature
h	10	W/(m^2 K)	natural convection heat transfer coefficient
σ_p	40	μS/cm	electric conductivity of tracing particles
a	0.5	Mm	radius of tracing particles

Thus, the speed of ETF may be estimated to scale as follows considering $\nabla T \sim \sigma \nabla E_f^2$ [18]:

$$U_{\mathrm{ET}} \sim \varepsilon_f \sigma E_f^4 \sim \varepsilon_f c E_f^4 \tag{21}$$

which is a quartic function of the applied electric field and gets stronger with increase of the fluid ionic concentration. The speed ratio between these two nonlinear electrokinetic flows is given by

$$\frac{U_{\mathrm{ET}}}{U_{\mathrm{ICEO}}} \sim \frac{\sqrt{\varepsilon_f}}{\varepsilon_w} c^{3/2} E_f^2, \tag{22}$$

which indicates the increasing dominance of ETF over ICEO in iDEP microdevices with the increase of fluid ionic concentration and/or electric field. This ratio also highlights the influences of the fluid and wall permittivity.

III. RESULTS AND DISCUSSION

A. Experimental images

Figure 2 shows the superimposed images of tracing particles in the constriction region of the microchannel in buffer solutions of varying concentrations under varying ac voltages. The dc voltage is fixed at 20 V. A smaller maximum ac voltage is used in the buffer solution with a higher concentration in order to keep the Joule heating effect from being intensive enough to damage the microchannel. In the low range of buffer concentrations from 0.01 to 0.1 mM, ICEO is observed under 300 V ac with the formation of stable fluid circulations near the opening of the constriction. With the increase of the ac voltage, these circulations first get stronger because of the quadratic dependence of ICEO on the electric field, leading to a local trapping and depletion of particles in the upstream and downstream zones of the constriction, respectively. They then start moving away from the opening towards the salient corners of the constriction and hence become weakened. This change is also accompanied by the reversed particle motion inside the constriction from along with

FIG. 2. Experimental images of tracing particles in a constricted microchannel in buffer solutions of different concentrations under different ac voltages. The dc voltage was fixed at 20 V and applied downwards. The arrow on each image indicates the particle moving direction inside the constriction, which switches from along the dc electric field (top to bottom) to against it with the increase of buffer concentration or ac voltage. The looped arrows on the top-left image highlight the fluid circulations of ICEO while those on both the top-right and bottom-left images highlight the fluid circulations of ETF.

the dc electric field to against it. Both phenomena are supposed to result from the development of ETF, whose velocity goes against that of ICEO and varies with the electric field at a higher-order dependence than ICEO. We will revisit this aspect later.

In the middle range of buffer concentrations including 0.25 and 0.5 mM, no apparent ICEO or ETF is observed under small ac voltages in Fig. 2. This should be due to the fact that the decreased EDL thickness reduces the polarization-induced zeta potential while the increased fluid conductivity is still insufficient to draw significant Joule heating effects. Increasing the ac voltage boosts the
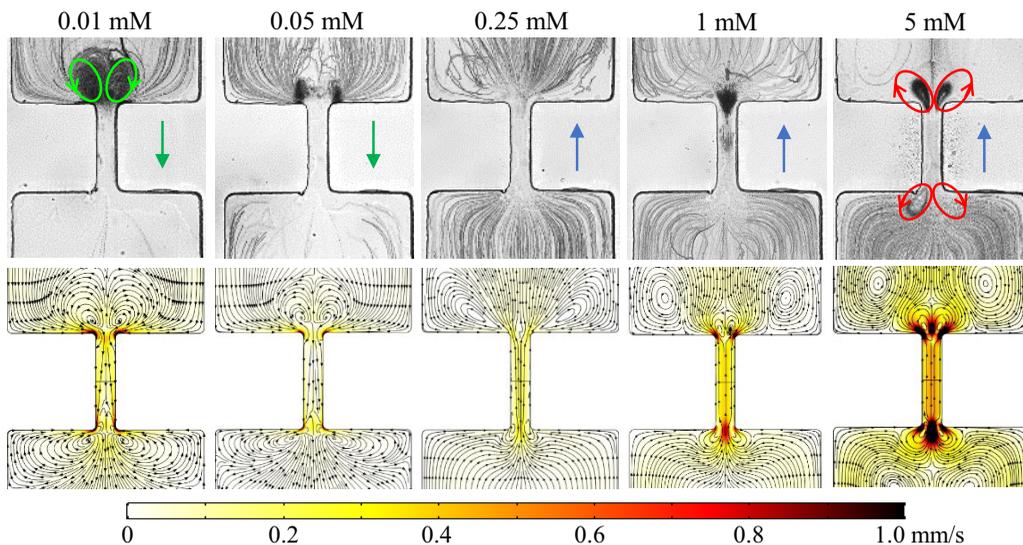
FIG. 3. Comparison of the experimentally (upper row) and numerically (lower row, the background color shows the magnitude of the particle velocity, the darker the larger) obtained particle streak lines in buffer solutions of different concentrations under a fixed 20-V dc-biased 500-V ac voltage. The arrow on each image indicates the particle moving direction inside the constriction, which switches from along the dc electric field (top to bottom) to against it with the increase of the buffer concentration because of the accompanying changes in the particle and wall zeta potentials. The looped arrows on the left-most and right-most images highlight the fluid circulations of ICEO and ETF, respectively.

ICEO, which is, however, suppressed and pushed towards the salient corners of the constriction by the much more quickly enhanced ETF. Therefore, there exists a relatively wide ac voltage span (which is from 0 to 600 V in 0.25-mM buffer) in the middle range of buffer concentrations, where no significant disturbances to the linear electroosmotic flow take place. For high buffer concentrations including 1 and 5 mM, ETF starts to form at the downstream size of the constriction and alters the local fluid motion even under low ac voltages (for example, 300 V in 5-mM buffer) because of the enhanced Joule heating effects in more conductive solutions. Increasing the ac voltage quickly strengthens the fluid circulations of ETF, leading to the electrothermal trapping of particles that has been recently demonstrated by our group [38,41]. In contrast, ICEO becomes insignificant and is not viewed in either 1- or 5-mM solution in Fig. 2. As noted above in the Experiment section, the tracing particles travel against the applied dc electric field in both the middle and high ranges of buffer concentrations because the particle zeta potential becomes greater than the wall zeta potential. In other words, the fluid circulations of ICEO and ETF trap particles in the upstream and downstream zones of the constriction, respectively, which are consistent with our earlier observations for each of the nonlinear electrokinetic fluid flows [35,38,41].

B. Effect of buffer concentration

Figure 3 compares the experimentally and numerically obtained streak lines of tracing particles in buffer solutions of different concentrations under a fixed 20-V dc-biased 500-V ac voltage. The model predicts the formation of ICEO in 0.01-mM buffer at both the entrance and exit of the constriction, whose strengths and patterns are, however, dissimilar because of the impact of the linear dc electroosmotic flow. The stronger fluid circulations of the upstream ICEO are observed in our experiment to trap and enrich the particles at the entrance of the constriction. Such trapping capability decreases with the increase of buffer concentration to 0.05 mM, where ICEO is
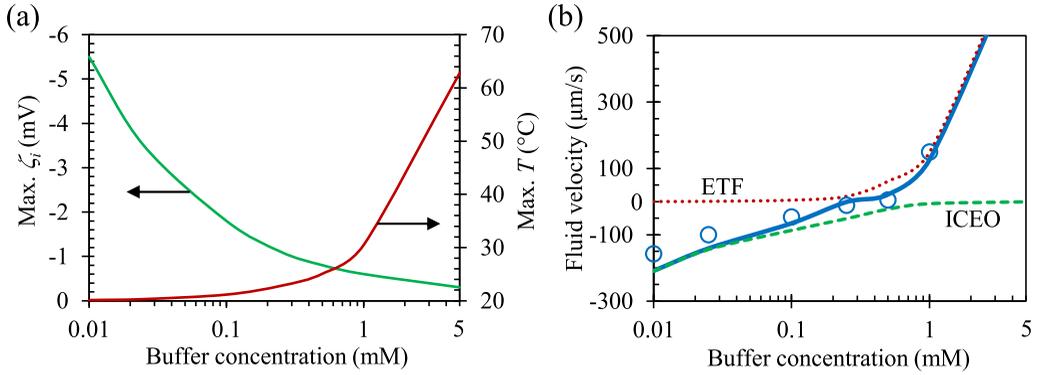
FIG. 4. Effect of buffer concentration on nonlinear electrokinetic flows in a constricted microchannel under a fixed 20-V dc-biased 500-V ac voltage: (a) Numerically predicted maximum induced zeta potential ζ_i (which occurs at approximately the starting point of the arc corner of the constriction entrance) and maximum fluid temperature T (which occurs in the middle of the constriction); (b) comparison of the experimentally (symbols) and numerically (solid line) obtained nonlinear fluid velocities (excluding the linear dc electroosmotic flow) along with the numerically predicted velocities of ICEO (with a negative velocity, dashed line) and ETF (with a positive velocity, dotted line) alone. The positive velocity is defined as that along the dc electric field.

weakened at both ends of the constriction because the reduced EDL thickness produces a smaller induced zeta potential ζ_i. ICEO gets even weaker in 0.25-mM buffer and fails to trap particles because of the continuously decreasing ζ_i with the increase of the buffer concentration as shown in Fig. 4(a). Moreover, the fluid circulations on the downstream side (with respect to the particle moving direction) are predicted to move away from the opening toward the salient corners of the constriction, which visually matches the experimental observation in Fig. 3.

Increasing the buffer concentration from 0.25 to 1 mM causes the development of ETF near each end of the constriction because the enhanced Joule heating is predicted to increase the maximum fluid temperature in the middle of the constriction from 22.8 to 30.5 °C [as compared to the 20 °C room temperature; see Fig. 4(a)]. This is also reflected by the observed greater rise in electric current with time (data not shown) due to the positive temperature dependence of the fluid conductivity [59,60]. Meanwhile, ICEO becomes insignificant and undistinguishable from the ETF-induced secondary fluid circulations in the salient corners of the constriction. The ETF circulates in a direction opposite to that of ICEO in the lower-concentration buffers. This may explain why the electrothermal trapping of particles is observed in our experiment (Fig. 3) to take place near the downstream opening (with respect to the particle moving direction) of the constriction while the ICEO-based particle trapping occurs upstream [note that the upstream and downstream sides swap because the electrokinetic particle motion reverses when the buffer concentration goes above 0.1 mM; see Eqs. (2) and (3)]. Note that our current model is unable to simulate the local particle trapping in ICEO or ETF, which can be implemented by solving the convection-diffusion equation to obtain the particle concentration field [38,41]. ETF gets much stronger in 5-mM buffer solution because of the significantly increased Joule heating effects [where the maximum fluid temperature becomes greater than 60 °C; see Fig. 4(a)], leading to an enhanced electrothermal trapping of particles as illustrated in Fig. 3. However, we notice increasing dissimilarities between the experimental and numerical images towards higher buffer concentrations. This may be ascribed to the slight changes in the used concentration and/or temperature dependences of fluid properties.

Figure 4(b) compares the experimentally and numerically obtained nonlinear fluid velocities along the centerline of the constricted microchannel with a 35-μm distance from the constriction opening. The experimental data were determined by subtracting the dc electrokinetic particle velocity from the measured particle velocity in each buffer solution in Fig. 3, where the former was
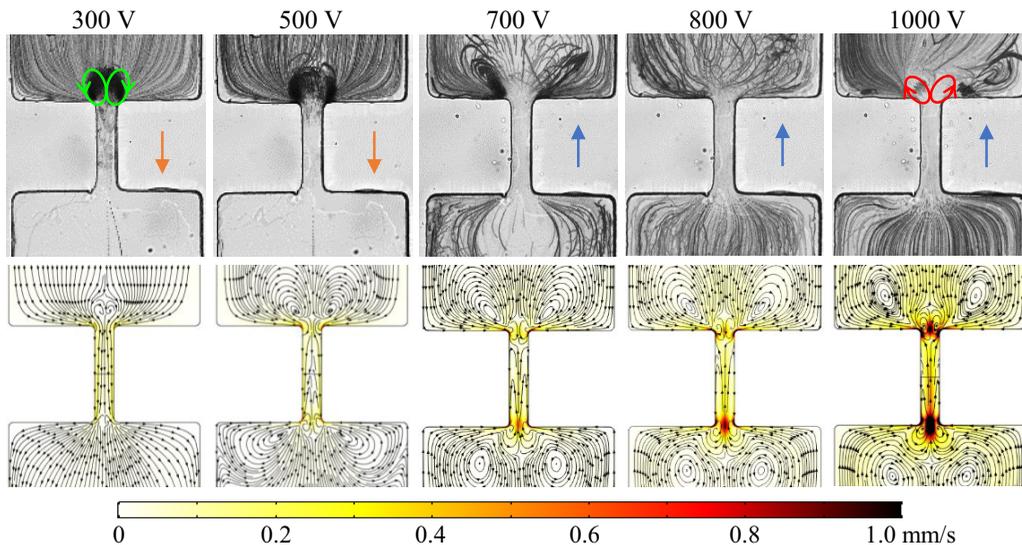
FIG. 5. Comparison of the experimentally (upper row) and numerically (lower row, the background color shows the magnitude of the particle velocity, the darker the larger) obtained particle streak lines in 0.1-mM buffer solution under different ac voltages. The dc voltage is fixed at 20 V. The arrow on each image indicates the particle moving direction inside the constriction, which switches from along the dc electric field (top to bottom) to against it with the increase of ac voltage because of the development of ETF. The looped arrows on the left-most and right-most images highlight the fluid circulations of ICEO and ETF, respectively.

obtained through multiplying the experimentally measured electrokinetic particle mobility by the numerically computed local dc electric field. The contribution of DEP to the particle velocity was neglected because the selected point is sufficiently distant from the region with strong electric field gradients. The numerical fluid velocity was set equal to $\mathbf{u}$ in Eq. (9) excluding the dc electroosmotic component that was obtained from $\mathbf{u}_{EO}$ at the local dc electric field. Overall the variation of the experimental fluid velocity with the buffer concentration agrees well with the curve of the numerical values in Fig. 4(b). Specifically, the nonlinear fluid velocity in low-concentration buffers matches asymptotically the numerically predicted velocity of ICEO alone (i.e., in the absence of Joule heating effects). In contrast, the nonlinear fluid velocity in high-concentration buffers matches asymptotically the numerically predicted velocity of ETF alone (i.e., in the absence of induced charge effects). These findings are consistent with the prediction of Eq. (22) from the scaling analysis. The nonlinear fluid velocity becomes marginal in moderate-concentration buffers (including 0.25 and 0.5 mM) because ICEO and ETF have opposing circulations and hence cancel the impact of each other.

C. Effect of ac electric field

Figure 5 compares the experimentally and numerically obtained particle streak lines in 0.1-mM buffer under the application of 20 V dc and different ac voltages. As predicted by the model, a pair of small fluid circulations of ICEO is observed experimentally at the entrance of the constriction under 300 V ac, which is capable of trapping the suspended particles upstream. No fluid circulations are predicted to form on the downstream side of the constriction because of the disturbance from the dc electroosmotic flow. With the increase of ac voltage to 500 V, ICEO becomes much stronger on the upstream side because of the increased value of ζ_i in Fig. 6(a). It is predicted to also form on the downstream side of the constriction as the enhanced fluid circulations dominate over the fixed dc electroosmotic flow. ICEO continues growing under 700 V ac because of the
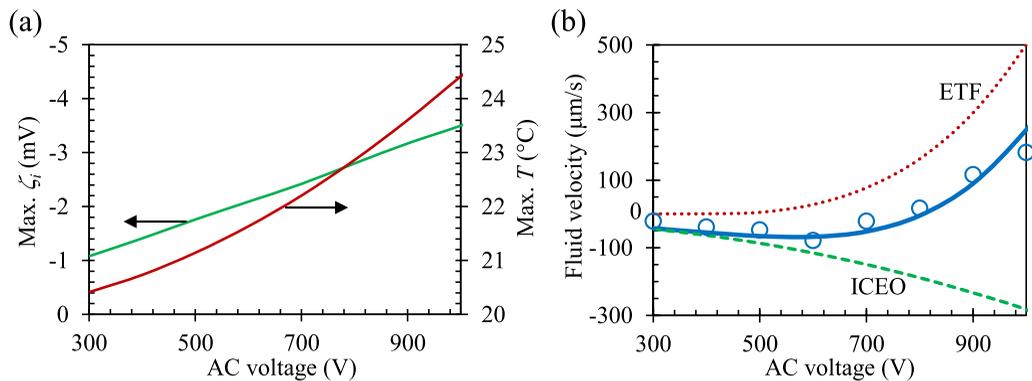
FIG. 6. Effect of the ac voltage on the nonlinear electrokinetic flow of 0.1-mM buffer in a constricted microchannel under a fixed 20-V dc: (a) Numerically predicted maximum induced zeta potential ζ_i and maximum fluid temperature T; (b) comparison of the experimentally (symbols) and numerically (solid line) obtained nonlinear fluid velocities (excluding the linear dc electroosmotic flow) along with the numerically predicted velocities of ICEO (with a negative velocity, dashed line) and ETF (with a positive velocity, dotted line) alone. The positive velocity is defined as that along the dc electric field.

increase of ζ_i with electric field in Fig. 6(a). Its fluid circulations, however, move away from the opening of the constriction and get weakened on either side, leading to the partial loss of particle trapping capability. Moreover, the particle traveling direction reverses inside the constriction. These phenomena result from the onset of ETF near the reentrant corners of the constriction because of the elevated local fluid temperature [22.2 °C as compared to the 20 °C room temperature in Fig. 6(a)]. As the ac voltage increases to 800 V, only weak fluid circulations of ICEO are observed downstream near the salient corners of the constriction. This pattern is visually similar to the experimental image for 0.25 mM buffer under 500-V ac in Fig. 3. Further increasing the ac voltage to 1000 V enhances the ETF whose fluid circulations are, however, still unable to trap particles because it is not strong enough (the maximum fluid temperature rise is less than 5 °C) and is counteracted by the ICEO.

Figure 6(b) compares the experimentally and numerically determined nonlinear fluid velocities along the channel centerline that were obtained using the same approach as that described above for the effect of buffer concentration. The measured fluid velocity agrees closely with the predicted value in the whole range of ac voltages. It becomes nearly equal to the predicted velocity of ICEO alone for small ac voltages (specifically, less than 500 V) because the ETF is marginal. Such an asymptotic matching is consistent with that in low-concentration buffer solutions in Fig. 4(b), where Joule heating effects also stay weak. The measured fluid velocity does not change significantly when the ac voltage increases from 500 to 700 V though the velocity magnitudes of ICEO and ETF both exhibit a high-order dependence on electric field. This is attributed to the competitive nature of the two nonlinear flows in the constriction region, which nearly cancel each other under 800-V ac leading to a marginal fluid velocity along the channel centerline. Such a state is analogous to that observed in moderate-concentration buffer solutions under 500-V ac in Fig. 4(b). For even higher ac voltages, the fluid velocity exhibits a similar trend with the ac voltage to that of the ETF alone but at a smaller magnitude. This indicates the dominance of ETF over the opposing ICEO because of the former flow's quicker increase with the electric field.

IV. CONCLUSIONS

We have performed an experimental, numerical, and theoretical analysis of the nonlinear fluid flow in a typical iDEP microdevice under dc-biased ac voltages. The observed flow pattern transits from ICEO to ETF as the buffer concentration and/or the ac voltage is increased. This trend is

consistent with a scaling analysis, and also properly simulated by the depth-averaged numerical model that considers both the electric polarization and Joule heating effects. Moreover, the experimentally obtained nonlinear fluid velocity agrees quantitatively with the numerical prediction in terms of buffer concentration and ac voltage dependence. We have also used the depth-averaged numerical model to isolate the two nonlinear electrokinetic effects, where the predicted velocities of ICEO and ETF match asymptotically the nonlinear fluid velocities in the low- and high-concentration buffers, respectively. Our results indicate that because of their opposing effects, the combination of the nonlinear ICEO and ETF has a minimal influence on the nonlinear iDEP of particles in moderate-concentration buffers under moderate ac voltages. This range of working parameters may be considered for a more accurate control of particles in iDEP microdevices. However, we admit that the proposed depth-averaged model is still inconvenient for other iDEP researchers to evaluate the impact of nonlinear electrokinetic flows on particle manipulation because their particle-device systems may be significantly different from ours in this work. We are currently building upon the proposed scaling analysis with the goal to define dimensionless numbers for estimating the relative magnitude of linear dc electrokinetic motion, nonlinear dc or ac electrokinetic flow, and nonlinear dc or ac DEP for particles of varying properties in iDEP devices.

[1] B. H. Lapizco-Encinas, On the recent developments of insulator-based dielectrophoresis: A review, Electrophoresis **40**, 358 (2019).

[2] P. Benhal, D. Quashie, Y. Kim, and J. Ali, Insulator based dielectrophoresis: Micro, nano, and molecular scale biological applications, Sensors **20**, 5095 (2020).

[3] B. H. Lapizco-Encinas, Microscale electrokinetic assessments of proteins employing insulating structures, Curr. Opin. Chem. Eng. **29**, 9 (2020).

[4] C. J. Ramirez-Murillo, J. M. de los Santos-Ramirez, and V. H. Perez-Gonzalez, Toward low-voltage dielectrophoresis-based microfluidic systems: A review, Electrophoresis **42**, 565 (2021).

[5] V. H. Perez-Gonzalez, Particle trapping in electrically driven insulator-based microfluidics: Dielectrophoresis and induced-charge electrokinetics, Electrophoresis (2021), doi:10.1002/elps.202100123.

[6] C. F. Chou and F. Zenhausern, Electrodeless dielectrophoresis for micro total analysis systems, IEEE Eng. Med. Biol. Mag. **22**, 62 (2003).

[7] E. B. Cummings, Streaming dielectrophoresis for continuous-flow microfluidic devices, IEEE Eng. Med. Biol. Mag. **22**, 75 (2003).

[8] S. K. Srivastava, A. Gencoglu, and A. R. Minerick, DC insulator dielectrophoretic applications in microdevice technology: A review, Anal. Bioanal. Chem. **399**, 301 (2010).

[9] J. Regtmeier, R. Eichhorn, M. Viefhues, L. Bogunovic, and D. Anselmetti, Electrodeless dielectrophoresis for bioanalysis: Theory, devices and applications, Electrophoresis **32**, 2253 (2011).

[10] X. Xuan, Recent advances in direct current electrokinetic manipulation of particles for microfluidic applications, Electrophoresis **40**, 2484 (2019).

[11] X. Xuan, Review of nonlinear electrokinetic flows in insulator-based dielectrophoresis: From induced charge to Joule heating effects, Electrophoresis (2021), doi:10.1002/elps.202100090.

[12] S. Thamida and H.-C. Chang, Nonlinear electrokinetic ejection and entrainment due to polarization at nearly insulated wedges, Phys. Fluids **14**, 4315 (2002).

[13] B. J. Hawkins and B. J. Kirby, Electrothermal flow effects in insulating (electrodeless) dielectrophoresis systems, Electrophoresis **31**, 3622 (2010).

[14] T. M. Squires and M. Z. Bazant, Induced-charge electro-osmosis, J. Fluid. Mech. **509**, 217 (2004).

[15] T. M. Squires and M. Z. Bazant, Induced-charge electrokinetic phenomena, Curr. Opin. Colloid Interface Sci. **15**, 203 (2010).

[16] A. Ramos, P. García-Sánchez, and H. Morgan, AC electrokinetics of conducting microparticles: A review, Curr. Opin. Colloid Interface Sci. **24**, 79 (2016).

[17] H. Feng, H. Chang, X. Zhong, and T. N. Wong, Recent advancement in induced-charge electrokinetic phenomena and their micro- and nano-fluidic applications, Adv. Colloid Interface Sci. **280**, 102159 (2020).

[18] A. Ramos, H. Morgan, N. G. Green, and A. Castellanos, Ac electrokinetics: A review of forces in microelectrode structures, J. Phys. D: Appl. Phys. **31**, 2338 (1998).

[19] N. G. Green, A. Ramos, A. González, A. Castellanos, and H. Morgan, Electric field induced fluid flow on microelectrodes: The effect of illumination, J. Phys. D: Appl. Phys. **33**, L13 (2000).

[20] A. Gonzalez, A. Ramos, H. Morgan, N. G. Green, and A. C. Castellanos, Electrothermal flows generated by alternating and rotating electric fields in microsystems, J. Fluid Mech. **564**, 415 (2006).

[21] P. Takhistov, K. Duginova, and H.-C. Chang, Electrokinetic mixing vortices due to electrolyte depletion at microchannel junctions, J. Colloid Interface Sci. **263**, 133 (2003).

[22] G. Yossifon, I. Frankel, and T. Miloh, On electro-osmotic flows through microchannel junctions, Phys. Fluid. **18**, 117108 (2006).

[23] Y. Eckstein, G. Yossifon, A. Seifert, and T. Miloh, Nonlinear electrokinetic phenomena around nearly insulated sharp tips in microflows, J. Colloid Interface Sci. **338**, 243 (2009).

[24] J. D. Sherwood, M. Mao, and S. Ghosal, Electrically generated eddies at an eightfold stagnation point within a nanopore, Phys. Fluids **26**, 112004 (2014).

[25] R. A. Prabhakaran, Y. Zhou, C. Zhao, G. Hu, Y. Song, J. Wang, C. Yang, and X. Xuan, Induced charge effects on electrokinetic entry flow, Phys. Fluids **29**, 062001 (2017).

[26] S. Sridharan, J. Zhu, G. Hu, and X. Xuan, Joule heating effects on electroosmotic flow in insulator-based dielectrophoresis, Electrophoresis **32**, 2274 (2011).

[27] R. Gallo-Villanueva, M. Sano, B. Lapizco-Encinas, and R. Davalos, Joule heating effects on particle immobilization in insulator-based dielectrophoretic devices, Electrophoresis **35**, 352 (2014).

[28] A. Kale, S. Patel, G. Hu, and X. Xuan, Numerical modeling of Joule heating effects in insulator-based dielectrophoresis microdevices, Electrophoresis **34**, 674 (2013).

[29] A. Kale, S. Patel, S. Qian, G. Hu, and X. Xuan, Joule heating effects on reservoir-based dielectrophoresis, Electrophoresis **35**, 721 (2014).

[30] R. A. Prabhakaran, Y. Zhou, S. Patel, A. Kale, Y. Song, G. Hu, and X. Xuan, Joule heating effects on electroosmotic entry flow, Electrophoresis **38**, 572 (2017).

[31] S.-C. Wang, H.-P. Chen, and H.-C. Chang, ac electroosmotic pumping induced by noncontact external electrodes, Biomicrofluid. **1**, 034106 (2007).

[32] S.-C. Wang, H.-P. Chen, C.-Y. Lee, C.-C. Yu, and H.-C. Chang, AC electro-osmotic mixing induced by non-contact external electrodes, Biosens. Bioelectron. **22**, 563 (2006).

[33] J. K. Chen and R. J. Yang, Vortex generation in electroosmotic flow passing through sharp corners, Microfluid. Nanofluid. **5**, 719 (2008).

[34] M. Zehavi and G. Yossifon, Particle dynamics and rapid trapping in electro-osmotic flow around a sharp microchannel corner, Phys. Fluid. **26**, 082002 (2014).

[35] H. Harrison, X. Lu, S. Patel, C. Thomas, A. Todd, M. Johnson, Y. Raval, T. Tzeng, Y. Song, J. Wang, D. Li, and X. Xuan, Electrokinetic preconcentration of particles and cells in microfluidic reservoirs, Analyst **140**, 2869 (2015).

[36] V. Chaurey, C. Polanco, C.-F. Chou, and N. S. Swami, Floating-electrode enhanced constriction dielectrophoresis for biomolecular trapping in physiological media of high conductivity, Biomicrofluidics **6**, 012806 (2012).

[37] A. Aghilinejad, M. Aghaamoo, X. Chen, and J. Xu, Effects of electrothermal vortices on insulator-based dielectrophoresis for circulating tumor cell separation, Electrophoresis **39**, 869 (2018).

[38] A. Kale, L. Song, X. Lu, L. Yu, G. Hu, and X. Xuan, Electrothermal enrichment of submicron particles in an insulator-based dielectrophoretic microdevice, Electrophoresis **39**, 887 (2018).

[39] G. Kunti, J. Dhar, A. Bhattacharya, and S. Chakraborty, Joule heating-induced particle manipulation on a microfluidic chip, Biomicrofluidics **13**, 014113 (2019).

[40] G. Kunti, T. Agarwal, A. Bhattacharya, T. K. Maiti, and S. Chakraborty, On-chip concentration and patterning of biological cells using interplay of electrical and thermal fields, Anal. Chem. **92**, 838 (2020).

[41] A. Malekanfard, Z. Liu, L. Song, A. Kale, C. Zhang, L. Yu, Y. Song, and X. Xuan, Joule heating-enabled electrothermal enrichment of nanoparticles in insulator-based dielectrophoretic microdevices, Electrophoresis **42**, 626 (2021).

[42] M. Zehavi, A. Boymelgreen, and G. Yossifon, Competition between Induced-Charge Electro-Osmosis and Electrothermal Effects at Low Frequencies around a Weakly Polarizable Microchannel Corner, Phys. Rev. Appl. **5**, 044013 (2016).

[43] Q. Wang, N. N. Dingari, and C. R. Buie, Nonlinear electrokinetic effects in insulator-based dielectrophoretic systems, Electrophoresis **38**, 2576 (2017).

[44] A. Malekanfard, C.-H. Ko, D. Li, L. Bulloch, A. Baldwin, Y.-N. Wang, L.-M. Fu, and X. Xuan, Experimental study of particle electrophoresis in shear-thinning fluids, Phys. Fluids **31**, 022002 (2019).

[45] A. Sze, D. Erickson, L. Ren, and D. Li, Zeta-potential measurement using the Smoluchowski equation and the slope of the current–time relationship in electroosmotic flow, J. Colloid Interface Sci. **261**, 402 (2003).

[46] B. J. Kirby and E. F. Hasselbrink, Zeta potential of microfluidic substrates: 1. Theory, experimental techniques, and effects on separations, Electrophoresis **25**, 187 (2004).

[47] B. J. Kirby and E. F. Hasselbrink, Zeta potential of microfluidic substrates: 2. Data for polymers, Electrophoresis **25**, 203 (2004).

[48] H. Lin, B. D. Storey, and J. G. Santiago, A depth-averaged electrokinetic flow model for shallow microchannels, J. Fluid Mech. **608**, 43 (2008).

[49] S. Ghosal, Lubrication theory for electro-osmotic flow in a microfluidic channel of slowly varying cross-section and wall charge, J. Fluid Mech. **459**, 103 (2002).

[50] L. Song, L. Yu, Y. Zhou, A. R. Antao, R. A. Prabhakaran, and X. Xuan, Electrokinetic instability in microchannel ferrofluid/water co-flows, Sci. Rep. **7**, 46510 (2017).

[51] A. Casterllanos, A. Ramos, A. Gonzalez, N. G. Green, and H. Morgan, Electrohydrodynamics and dielectrophoresis in microsystems: Scaling laws, J. Phys. D: Appl. Phys. **36**, 2584 (2003).

[52] G. Yossifon, I. Frankel, and T. Miloh, Macro-scale description of transient electro-kinetic phenomena over polarizable dielectric solids, J. Fluid Mech. **620**, 241 (2009).

[53] C. Zhao and C. Yang, Analysis of induced-charge electro-osmotic flow in a microchannel embedded with polarizable dielectric blocks, Phys. Rev. E **80**, 046312 (2009).

[54] C. Zhao and C. Yang, AC field induced-charge electroosmosis over leaky dielectric blocks embedded in a microchannel, Electrophoresis **32**, 629 (2011).

[55] J. R. Melcher and G. I. Taylor, Electrohydrodynamics: A review of the role of interfacial shear stresses, Annu. Rev. Fluid Mech. **1**, 111 (1969).

[56] D. Li, *Electrokinetics in Microfluidics* (Elsevier Academic, Burlington, MA, 2004).

[57] H.-C. Chang and L. Y. Yeo, *Electrokinetically Driven Microfluidics and Nanofluidics* (Cambridge University Press, New York, 2010).

[58] L. Song, L. Yu, C. Brumme, R. Shaw, C. Zhang, and X. Xuan, Joule heating effects on electrokinetic flows with conductivity gradients, Electrophoresis **42**, 967 (2021).

[59] X. Xuan, Joule heating in electrokinetic flow, Electrophoresis **29**, 33 (2008).

[60] B. Cetin and D. Li, Effect of Joule heating on electrokinetic transport, Electrophoresis **29**, 994 (2008).